Materials Today Bio 29 (2024) 101261

Contents lists available at ScienceDirect

Materials Today Bio

journal homepage: www.journals.elsevier.com/materials-today-bio

# Functionalized 3D-printed GelMA/Laponite hydrogel scaffold promotes BMSCs recruitment through osteoimmunomodulatory enhance osteogenic via AMPK/mTOR signaling pathway

Linquan Zhou [a,1], Chengcheng Zhang [c,1], Tengbin Shi [a,1], Dingwei Wu [a,1], Huina Chen [c], Jiaxin Han [c], Dehui Chen [a], Jinxin Lin [b], Wenge Liu [a,*]

[a] Fujian Medical University Union Hospital, Fuzhou, 350000, China
[b] Key Laboratory of Optoelectronic Materials Chemistry and Physics, Fujian Institute of Research on the Structure of Matter, Chinese Academy of Sciences, Fuzhou, 350000, China
[c] The School of Health, Fujian Medical University, Fuzhou, 350000, China

ARTICLE INFO

*Keywords:*
3D-printed
Hydrogel
Apt19s
AMPK/mTOR signaling pathway
Osteoimmunomodulatory

ABSTRACT

The migration and differentiation of bone marrow mesenchymal stem cells (BMSCs) play crucial roles in bone repair processes. However, conventional scaffolds often lack of effectively inducing and recruiting BMSCs. In our study, we present a novel approach by introducing a 3D-bioprinted scaffold composed of hydrogels, with the addition of laponite to the GelMA solution, aimed at enhancing scaffold performance. Both *in vivo* and *in vitro* experiments have confirmed the outstanding biocompatibility of the scaffold. Furthermore, for the first time, Apt19s has been chemically modified onto the surface of the hydrogel scaffold, resulting in a remarkable enhancement in the migration and adhesion of BMSCs. Moreover, the scaffold has demonstrated robust osteogenic differentiation capability in both *in vivo* and *in vitro* environments. Additionally, the hydrogel scaffold has shown the ability to induce the polarization of macrophages from M1 to M2, thereby facilitating the osteogenic differentiation of BMSCs via the bone immune pathway. Through RNA-seq analysis, it has been revealed that macrophages regulate the osteogenic differentiation of BMSCs through the AMPK/mTOR signaling pathway. In summary, the functionalized GelMA/Laponite scaffold offers a cost-effective approach for tailored in situ bone regeneration.

## 1. Introduction

Treating large bone defects, often encountered in severe trauma and after tumor surgery, poses a significant challenge for orthopedic surgeons. Currently, the primary methods for filling bone defects involve autogenous bone grafts and allogeneic bone grafts. However, for complex bone defects, simple filling methods often fall short of achieving effective treatment [1]. Nowadays, the development of 3D printing can overcome some shortcomings of customization of treatments and provided functional tissues capable of replacing in humans [2]. This technique makes it a promising solution for addressing the limitations of autogenous and allograft bone grafts [3,4]. Meanwhile, the components in 3D bioprinted constructs can directly mediate the differentiation phenotype of cells [5]. Currently, we can choose different kinds of materials for bone regeneration, include polymers, hydrogel and metal organic frameworks (MOFs) [6–8]. Hydrogel has been one of the most promising biomaterials in bone regeneration. Moreover, hydrogel scaffolds often lack bone inductivity and possess inadequate mechanical strength, which is one of the major limitations of hydrogel in the treatment of bone defect.

The key of tissue repair is in situ regeneration of lesion cells, so as to achieve lesion repair and regeneration [9]. GelMA encompasses RGD sequences (Arg-Gly-Asp peptides), which promoting cell adhesion. However, RGD peptides may be easily degrade by matrix metalloproteinase enzyme and resulting in decreased cell adhesion. We coupled the Apt19s, a nucleic acid aptamer targeting stem cells, to the surface of GelMA scaffold through chemical methods, which can avoid the degradation of enzymes. Compared with other methods, this

* Corresponding author.
*E-mail address:* wengeunion@fjmu.edu.cn (W. Liu).
[1] These authors contributed equally to this work.

https://doi.org/10.1016/j.mtbio.2024.101261
Received 30 May 2024; Received in revised form 4 September 2024; Accepted 19 September 2024
Available online 23 September 2024

chemical modification shows better stability [10]. To enhance bone tissue regeneration treatment strategies, aptamer and fusion protein pBMP2 were separately modified on the surface of porous scaffolds. The sequential delivery of two biologically active molecules serves a dual purpose. Firstly, Apt19s facilitates the mobilization and recruitment of host endogenous BMSCs to the fracture defect site. Secondly, the slow and sustained release of BMP-2 can induce osteogenic differentiation of BMSCs. The sequential release system has shown promising bone regeneration capabilities in both *in vivo* and *in vitro* studies [11,12]. Inspired by this, we modified Apt19s on the GelMA scaffold surface by chemical method to achieve BMSCs targeted recruitment.

To address the lack of bone inductivity and possess inadequate mechanical strength. Incorporating inorganic materials not only enhances the mechanical properties and compression resistance of the scaffold but also triggers bone differentiation of BMSCs [13,14]. Laponite (Lap) is one of promising osteoinductive additive which can maintain the osteogenic differentiation capability of BMSCs. Furthermore, they enhance cell adhesion, proliferation and osteogenic differentiation, consequently promoting bone regeneration in a dose-dependent manner [15,16]. The released $Mg^{2+}$ also have immunomodulatory effects. The immune cell especially macrophages may play a role in regulating bone regeneration through various factors such as cytokines and extracellular vesicles [17–19]. These cytokines can be stimulated by materials or gut microbiota, then enhance osteoclast activity in the later stages of fracture healing [20,21]. M2 macrophages can stimulate osteogenic differentiation of MSCs. This process is regulated by various biological pathways such as the Wnt pathway, MAPK pathway, and AMPK pathway [22–24].

Studies have shown that AMPK singing pathway plays an important role in regulating bone regeneration. In the diabetic rat model, researchers found that PPARβ/δ agonist promotes osteogenic differentiation of rBMSCs through AMPK/mTOR singing pathway [25]. Supplementation of magnesium can not only affect the polarization of macrophages, but also regulate autophagy through mTOR [26]. In addition, $Mg^{2+}$ coated Ti6Al4V scaffolds has been demonstrated promote autophagy in osteosarcoma by activating the AMPK/mTOR signaling pathway [27]. However, Mg2+ is one of the main elements of Lap. Specific studies aiming to determine whether GelMA/Lap scaffold promote osteogenesis and the signaling pathways through which this effect is induced are needed.

This study involved incorporating various concentrations of Laponite to GelMA hydrogel for 3D printing purposes. For the first time, Apt19s was modified onto the surface of the scaffold, and the physicochemical properties of the composite scaffold were subsequently characterized and analyzed. *In vitro* assessments were conducted to evaluate the biocompatibility, bone induction capability, regulation of macrophage polarization, and efficiency of BMSCs recruitment of the functionalized hydrogel scaffolds. Additionally, the bone regeneration efficiency was evaluated using an SD rat skull defect model. Concurrently, we utilized RNA-seq transcriptome sequencing analysis to investigate the potential biological mechanism of bone regeneration via bone immune regulation, employing molecular biology techniques (Scheme 1). These findings aim to offer therapeutic strategies and a theoretical foundation for future bone repair therapies.

## 2. Result and discussion

### 2.1. Preparation and characterization of functional 3D printed hydrogel scaffolds

3D printing offers significant technical support for the treatment of large-area bone defects. Hydrogel materials exhibit superior biocompatibility and degradability compared to traditional polymers. The utilization of bio-ink with hydrogel in 3D printing demonstrates promising application prospects [28,29]. Biological 3D printing utilizing GelMA has garnered widespread application in bone tissue engineering. The active groups on its surface allow for various functional modifications to

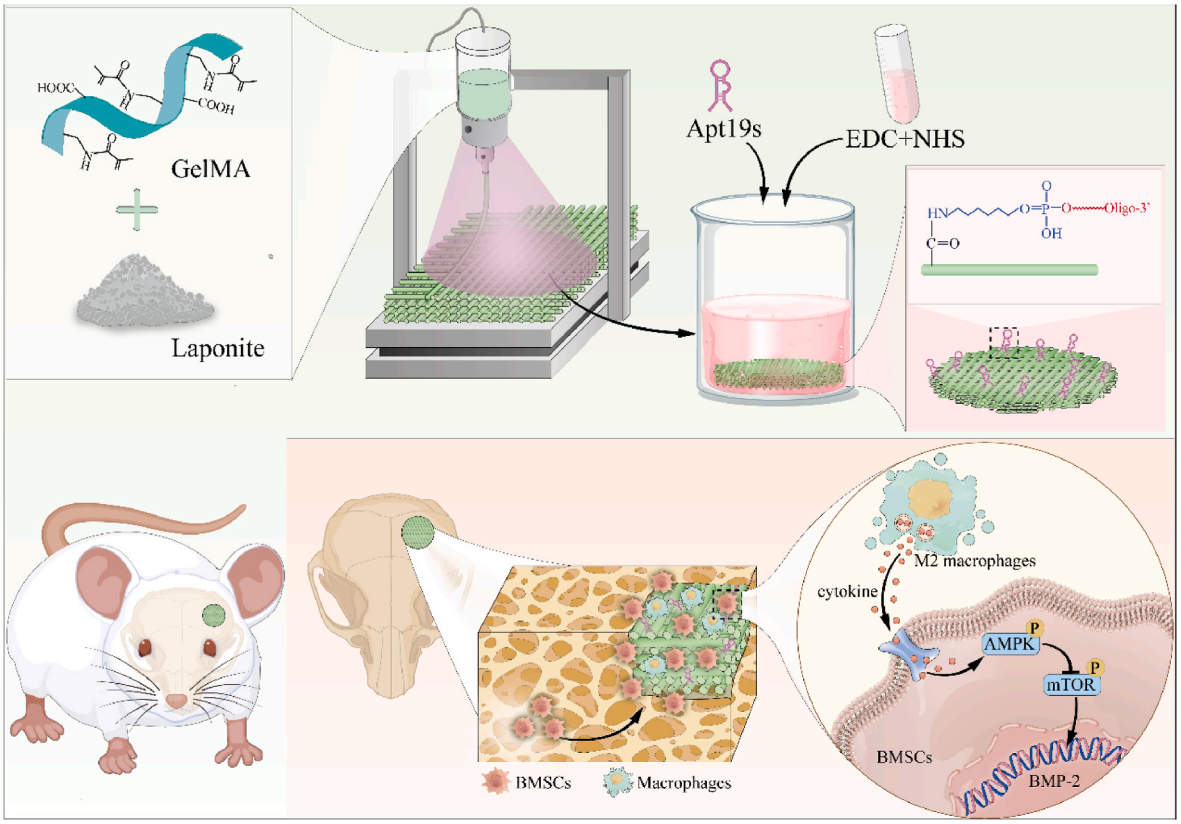


**Scheme 1.** Mechanism schematic illustration of functionalized 3D-printed GelMA/Laponite hydrogel scaffold for bone tissue regeneration.

be achieved. In this study, GelMA/Laponite hydrogel scaffolds were 3D-printed. The surface carboxyl groups of GelMA were activated using EDC and NHS, following which Apt19s were modified onto the scaffolds. As depicted in Fig. 1A, GelMA alone exhibits poor continuity during the printing process owing to its low viscosity. Irregular spacing within the support structure and local breakage are common issues. However, upon the addition of varying concentrations of Laponite, the printed scaffolds demonstrate improved continuity. When the concentration of Laponite reached 8 %, the hydrogel was continuously extruded **(Video,** Supporting **Information)**. Additionally, the spacing within the scaffold appeared relatively regular. This improvement can be attributed to the ability of Laponite to increase the overall viscosity of the hydrogel material, thereby enabling it to maintain its shape effectively during the extrusion printing process. Additionally, different hydrogel composites were performed by rheological tests and it shows the storage modulus of GelMA/Laponite exceeds the loss modulus by nearly an order of magnitude in the frequency scanning range. Among them, the storage modulus of hydrogel containing 8 % Laponite is largest (Fig. 1D). These results indicate that the increase of Laponite concentration is beneficial to the shape maintenance of the extruded fluid.

Hence, Laponite-doped composite materials hold promise for applications across various types of tissue and organ 3D printing materials, including tumor organs and bone tissue 3D printing [30,31]. SEM results revealed that the addition of Laponite did not alter the "honeycomb" structure of the hydrogels, as observed in the cross-sectional morphology of different groups. However, it was observed that the overall porosity of GelMA/Laponite was reduced, and the thickness between the pores increased. Subsequently, the hydrogel containing 8 % Laponite underwent scanning for five different elemental contents using EDS-Mapping, revealing that C and O still dominated the composition. Additionally, Si and Mg were detected at 6.95 % and 4.29 %, respectively, along with a small amount of Ca (Fig. S1). In particular, Mg may enhance the osteogenic differentiation of BMSCs by activating the PI3K/Akt signaling pathway during degradation from Laponite [16]. We also found that the $Mg^{2+}$ released by the scaffold with the time increased (Fig. 1E). On the other hand, it also promotes peripheral vascular regeneration and facilitating bone repair [32]. Consequently, the addition of Laponite renders the hydrogel scaffolds potentially osteoinductive.

To examine the impact of adding different concentrations of Laponite to the GelMA hydrogel, we initially detected the changes in absorption peaks of the samples using FTIR. The results show significant peaks were observed in Laponite alone at 1007 $cm^{-1}$ and 656 $cm^{-1}$, corresponding to the Si-O stretching vibration and Mg-OH-Mg vibration, respectively. Similarly, these two characteristic peaks were also clearly detected in GelMA/3 % Lap and GelMA/8 % Lap, which is in line with previous

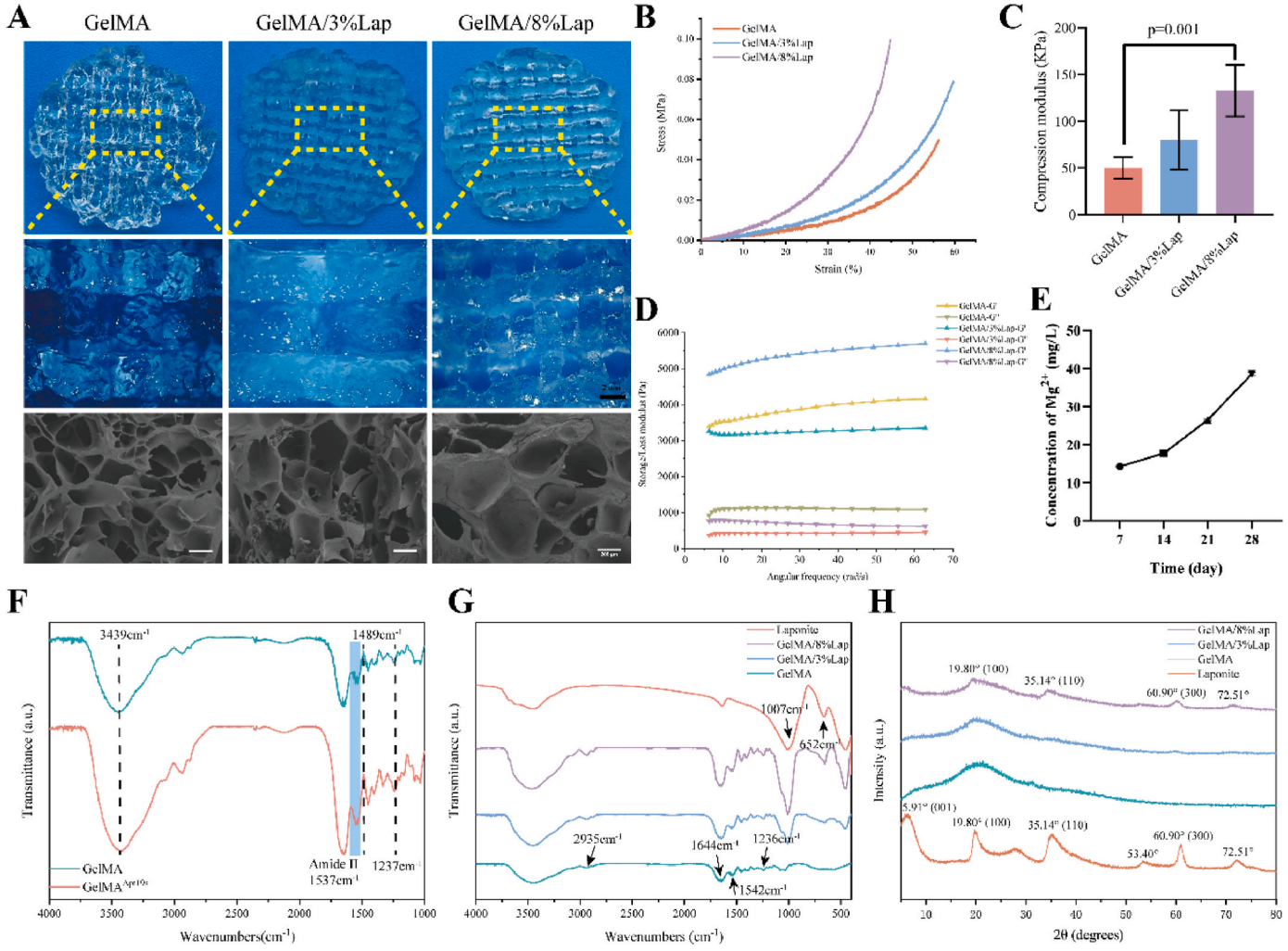


**Fig. 1.** Characterization of hydrogel scaffold. A. Photograph displaying the 3D-printed hydrogel scaffold along with a SEM image; B. Mechanical properties of the hydrogel scaffolds, including stress-strain analysis; C. Evaluation of compressive modulus for the hydrogel scaffolds; D. Frequency sweep measurements of the different hydrogels; E. $Mg^{2+}$ release from GelMA/8%Lap hydrogel scaffold; F. FTIR spectra between GelMA and $GelMA^{Apt19s}$; G. FTIR spectra of GelMA, Laponite, GelMA/3%Lap, and GelMA/8%Lap; H. XRD spectra of GelMA, Laponite, GelMA/3%Lap, and GelMA/8%Lap.

literature reports [33]. In the simple GelMA scaffold, peaks at 2935, 1644, 1542, and 1236 $cm^{-1}$ were associated with the C-H stretching of alkyl groups, C=O stretching of the amide I band, N-H stretching of amide II band, and N-H stretching of amide III band, respectively (Fig. 1G). These absorption peaks were retained after the addition of Laponite, indicating that Laponite primarily relies on physical adsorption within GelMA. To investigate whether -$NH_2$-Apt19s can be modified on the surface of GelMA, we initially conducted FTIR experiments. The result revealed the presence of modified GelMA at 1537 $cm^{-1}$ in the amide bond II band, characterized by an observable peak darkening (Fig. 1F). This suggests a potential reaction between Apt19s and GelMA in that region. Consistently, a characteristic absorption peak near 1540 $cm^{-1}$ was observed, similar to when the same DNA structure was introduced into the porous GelMA [34]. Furthermore, we observed the retention of specific absorption peaks for GelMA at 3489 $cm^{-1}$, 1489 $cm^{-1}$ and 1237 $cm^{-1}$. Typically, aptamers with lengths ranging from 6 to 30 kDa have average diameters of less than 5 nm [35]. Consequently, we investigated the distribution of Apt19s within the gel using laser confocal microscopy after incubating FITC-Apt19s with simple GelMA scaffolds. The results demonstrated that Apt19s could be evenly distributed throughout the hydrogel (Fig. S2). This ensures that the scaffolds are thoroughly modified by Apt19s rather than just surface-modified. As a result, Apt19s can effectively recruit BMSCs for migration continuously. At the same time, this chemical modification allows the aptamer to better bind to the scaffold.

Then, we investigated the internal crystal structure of the composite hydrogel using XRD, which was scanned for different samples. The results revealed that for simple Laponite, the 2θ angles were 5.91°, 19.80°, 35.14°, and 60.90°, corresponding to crystal planes (001), (100), (005), (110), and (300), respectively. In the GelMA and GelMA/3 % Lap groups, no significant diffraction peaks were detected. However, in the GelMA/8 % Lap group, diffraction peaks were observed at 5.91° (001), 35.14° (100), 60.90° (300), and 72.51° (Fig. 1H). These diffraction peaks were largely consistent with those of Laponite without significant shift, suggesting that the crystal structure of Laponite was maintained within the composite hydrogel. Given that Laponite is a nanoparticle with a layered structure, it can utilize surface electrostatic interactions to adsorb drugs and other substances. No significant diffraction was detected in the 3 % Laponite group, likely attributed to the shear force generated by the stirring action during the preparation process. This could disrupt its lamellar structure, leading to a change in d-spacing. While a 3D-printed hydrogel scaffold may not offer robust mechanical support, it is still required to provide some level of mechanical strength during practical application. It should be able to withstand the extrusion forces exerted by surrounding soft tissues and provide support for tissue growth. During the preparation process, the addition of Laponite enhanced the mechanical properties of GelMA scaffolds to some degree. Subsequently, we conducted mechanical compression experiments using using groups of scaffolds. The findings indicated that the compression modulus was highest for scaffolds containing an 8 % Laponite concentration, averaging 132.5 KPa (Fig. 1B and C). In comparison, GelMA alone exhibited an average compression modulus of 50 kPa. One possible explanation for these results is the electrostatic interactions between gelatin and clay, which enhance the compressive properties of the hydrogel. Additionally, the interaction between GelMA and clay molecules synergistically increases the mechanical strength of the gels [36,37]. This presents opportunities for its application in bone tissue engineering. Apt19s is a single-stranded DNA molecule with a length of only 49 base pairs. Utilizing the hydroxyl group at the 5′ end of the phosphate terminus, the amino group is coupled to an aptamer. This enables its utilization for functionalized modification of hydrogel scaffolds.

### 2.2. Biocompatibility and recruitability of Apt19s functionalized hydrogel scaffolds

The composition of the hydrogel can significantly impact the biological activity of endogenous cells, including stem cell adhesion, proliferation, and osteoblast differentiation. These factors are influenced by the degradation and ion release of the gel material [38]. To investigate the impact of varying concentrations of Laponite on BMSCs growth, we initially cultured BMSCs with different hydrogel extracts for 1 day and 3 days, followed by staining them with live/dead markers. The result revealed no significant cell death observed on day 1 after the culture of BMSCs, with the cells displaying a rounded appearance at this time. The cells exhibited a spindle-shaped structure on day 3. Notably, in the 8 % Laponite group, there was an increase in the number of cells compared to the control group (Fig. S3). Elements such as Li, Si, and Mg released by the degradation of Laponite demonstrate minimal cytotoxic effects and can promote the induction of osteogenic differentiation [39,40]. Subsequently, three groups of hydrogel stents were implanted into the subcutaneous tissue of rats, and histological examination using HE staining was conducted on the 10th and 20th day after surgery (Fig. S4). The results revealed a significant proliferation of tissue cells along the hydrogel scaffold in each group, with no apparent tissue liquefaction or necrosis observed. These findings indicate that the hydrogel scaffolds maintained good biological compatibility even after the addition of different concentrations of Laponite.

The key aspect in achieving bone repair lies in increasing the number of MSCs within the scaffold, and Apt19s has been noted for its high affinity for stem cells. Researchers identified this phenomenon by modifying Apt19s on the surface of the PCL scaffold in a rat model of meniscus damage. They found at a concentration of 1 nM showed no promoting effects on BMSCs migration. Notably, when the concentrations of Apt19s increased to 10 nM and 100 nM, the results showed no significant difference, which indicating that 10 nM Apt19s might be sufficient for enhancing BMSCs migration [41]. To validate the affinity of Apt19s to BMSCs, the binding rate of Apt19s to BMSCs reached 97.3 % (Fig. 2A and B). The results were consistent with previous reports, confirming that Apt19s exhibit a high affinity for MSCs [42]. Then, BMSCs were seeded onto the surface of the GelMA scaffold modified with Apt19s, and the cell adhesion effect was observed using fluorescence microscopy. The results revealed a significant increase in the number of cells on the GelMA scaffold modified with Apt19s. Confocal laser microscopy further illustrated that BMSCs spread out well, forming irregular structures (Fig. 2C and D). The results of the Transwell experiment demonstrated a significant increase in the number of migrated cells after Apt19s modification compared to unmodified scaffolds. Interestingly, the chemotactic effect of Apt19s on BMSCs remained unaffected even after the addition of Laponite (Fig. 2E and F). This suggests that the surface charge of Laponite does not influence the biological function of Apt19s.

### 2.3. Hydrogel induced macrophage polarization

The differentiation of BMSCs, a biological process, primarily governs bone regeneration. Recent research highlights the significant role of immune cells, particularly macrophages, in regulating this process. Based on this understanding, there has been a continuous effort to develop biomaterials with immunomodulatory effects on bone [43]. The researchers incorporated xonotlite nanofiber into a 3D-printed fibroin protein hydrogel scaffold. Through the influence of Ca, Si, and other inorganic elements, effective bone regeneration and regulation of the bone immune microenvironment were achieved [44]. Furthermore, Laponite also contains Si and other elements. Therefore, the aim was further to investigate the regulatory effects of GelMA/8%Lap on bone immunity. Initially, we assessed the alterations of CD86 and CD206 in bone marrow primary macrophages following intervention with hydrogel extract using flow cytometry. The findings revealed that in the

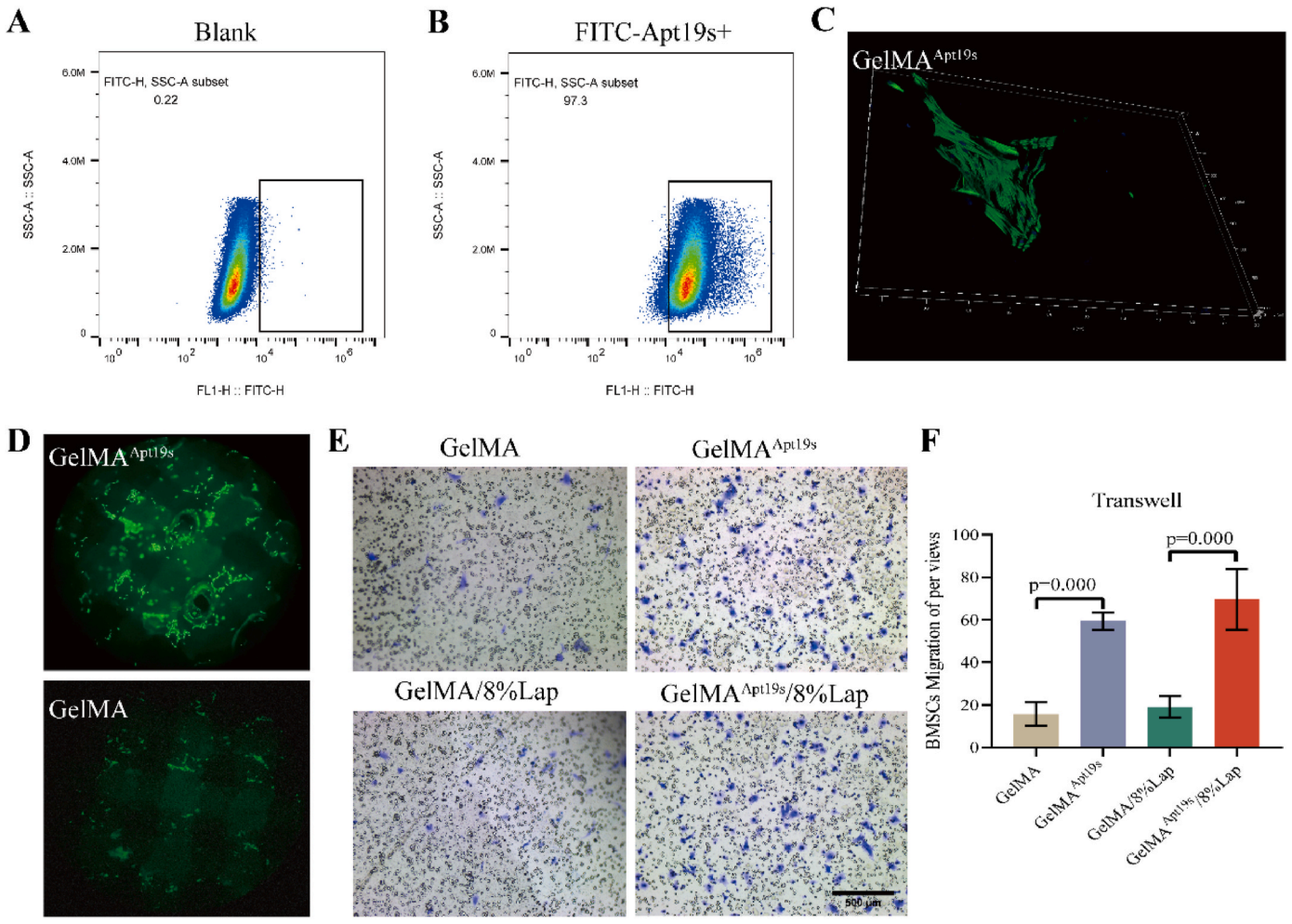


**Fig. 2.** Evaluation of Apt19s specific binding and recruitment ability on BMSCs. (A) Flow cytometry analysis illustrating Apt19s binding. (B) Flow cytometry analysis demonstrating the binding of FITC-labeled Apt19s. (C) Confocal immunofluorescence microscopy images depicting BMSCs adhesion to the GelMA$^{Apt19s}$ hydrogel scaffold. (D) Immunofluorescence microscopy images showing BMSCs adhesion to the GelMA$^{Apt19s}$ and GelMA hydrogel scaffolds. (E) Statistical analysis of BMSCs migration towards different groups, including GelMA, GelMA$^{Apt19s}$, GelMA/8%Lap, and GelMA$^{Apt19s}$/8%Lap groups in a Transwell system. (F) Crystal staining assessment of BMSCs migration towards the GelMA, GelMA$^{Apt19s}$, GelMA/8%Lap, and GelMA$^{Apt19s}$/8%Lap groups in a Transwell system.

RM2 group, the proportion of CD206 increased from 1.74 % to 18.8 %, while the proportion of CD86 decreased from 73.8 % to 69.5 % (Fig. 3A and B). Importantly, Laponite demonstrated the ability to revert macrophages from an M1-type and promote their transition to an M2-type. Furthermore, we assessed the expression of genes linked to inflammation using PCR. The findings indicated that in the RM2 group, the expression of anti-inflammatory factors Arg-1 and IL-10 decreased compared to M2-type macrophages but remained lower than that observed in M1-type macrophages. Conversely, the expressions of iNOS and IL-1 genes in M1-type macrophages were notably higher than those observed in M2-type macrophages (Fig. 3C and D). Additionally, we conducted immunofluorescence analysis to observe the expression of CD86 and CD206 in primary macrophages. The findings revealed that the expression of CD86 was lower compared to that of M1-type macrophages, while the expression of CD206 was higher than that of M1-type macrophages (Fig. S5).

Subsequently, we investigated the regulation of local inflammation by composite hydrogel scaffolds through *in vivo* experiments (Fig. 3E). We observed a notable presence of CD86-positive cells, particularly evident in the GelMA group after subcutaneous implantation at 10 days. Conversely, the GelMA/8%Lap group exhibited significantly lower expression of CD86-positive cells compared to the GelMA group. Also, the proportion of CD206 positive cells in the GelMA/8%Lap group was markedly higher than that in the GelMA group. By day 20, although CD86 positivity remained higher in the GelMA group, the overall level had decreased compared to day 10. Similarly, the expression of CD206 in each group was most pronounced on the 10th day after surgery (Fig. 3F–H). This observation suggests that the inflammation regulation mediated by the hydrogel scaffold primarily takes place during the early stages of injury, aligning well with the bone repair process. During the initial phase of injury, various immune cells, predominantly macrophages surrounding the bone tissue, become activated. Through the secretion of biological factors, these cells initiate the process of osteogenic differentiation in stem cells [45,46].

### 2.4. Hydrogel scaffold-mediated osteogenic differentiation induction

3D printing with GelMA hydrogel as bio-ink has been extensively employed in bone repair projects. Despite GelMA inherent lack of robust bone induction functionality, PRP is loaded in the 3D-printed GelMA scaffold utilizing the unique pore structure of the hydrogel. The experimental findings indicate that this approach enhances the scaffold's bone repair capability [47]. The study revealed a positive correlation between the increase in Laponite concentration and the activity of MC3T3 cells to express ALP, even at concentrations ranging from 5 % to 25 %, Laponite exhibited no apparent cytotoxicity and emerged as a potential osteogenic induction additive [48]. However, it is important to note that biological factors are susceptible to denaturation and

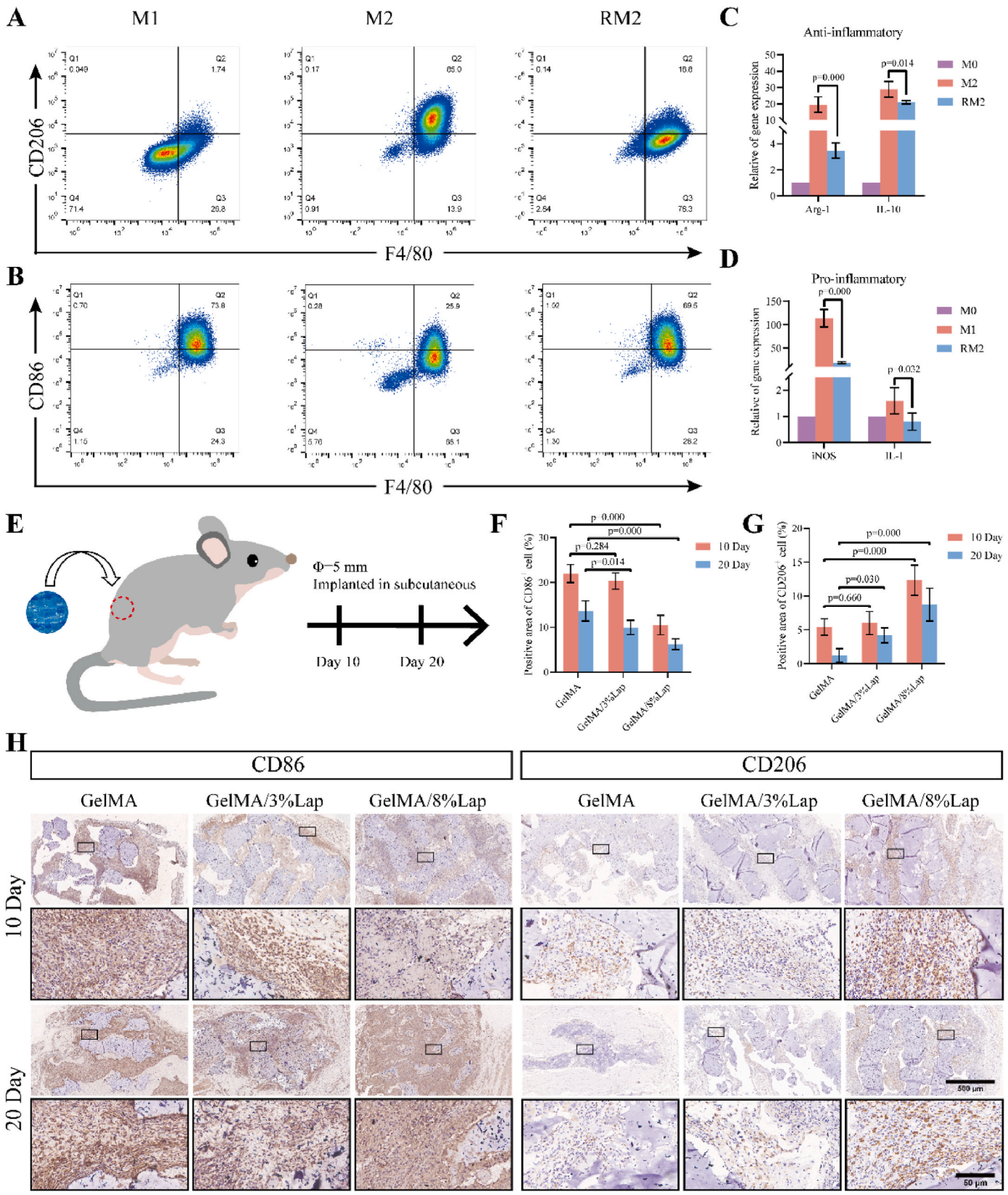


**Fig. 3.** Promotion of macrophage reprogramming by 3D-printed GelMA/8%Lap scaffold: A. Flow cytometry analysis showing co-localization of M1, M2, and RM2 macrophages using F4/80 and CD206. B. Flow cytometry analysis demonstrating co-localization of M1, M2, and RM2 macrophages using F4/80 and CD86. C. qRT-PCR analysis of mRNA levels of Arg-1 and IL-10 in M0, M2, and RM2 macrophages. D. qRT-PCR analysis of mRNA levels of iNOS and IL-1 in M0, M2, and RM2 macrophages. E. Schematic illustration depicting scaffold implantation in subcutaneous tissue. F. Quantitative analysis of CD86 positive cells in the area. G. Quantitative analysis of CD206 positive cells in the area; H. Immunohistochemical staining image of CD86 and CD206 for the hydrogel scaffold implantation in subcutaneous tissue.

deactivation during the printing process, leading to a reduction in biological efficiency. The composite hydrogel bio-ink, prepared by doping inorganic elements such as hydroxyapatite, also exhibits a favorable osteogenic effect [49]. In this study, the bone induction capability of composite hydrogel scaffolds was examined. Initially, three hydrogel extracts were utilized for BMSCs culture, followed by ALP staining on days 7 and 14. Results revealed that ALP staining in the group containing 8 % Laponite was notably deeper compared to GelMA alone. Moreover, ALP staining was most prominent in the 8 % Laponite group on day 14 (Fig. 4A).

To further validate the osteogenic effect of the composite hydrogel scaffold, the expression of osteogenic genes in MC3T3 and BMSCs was assessed via PCR. The results demonstrated that the expressions of Col, Runx2, OPN, and OCN genes in the GelMA/8%Lap group were significantly higher compared to those in the GelMA/3%Lap group on the 7th day of BMSCs culture. However, only OCN expression was significantly higher in the GelMA/3%Lap group. On the 14th day, it was observed that the expressions of Col, Runx2, OPN, and OCN genes were significantly increased in the GelMA/8%Lap group. However, in the GelMA/3%Lap group, only Col1 and Runx2 showed significant increases (Fig. 4B and C). For MC3T3, on the 7th day of culture, expressions of Col1 and OPN genes significantly increased in the GelMA/8%Lap group, while only OCN significantly increased in the GelMA/3%Lap group. On the 14th day, the expressions of Col1, OCN, and OPN genes significantly increased in the GelMA/8%Lap group, whereas only Col1 and OPN significantly increased in the GelMA/3%Lap group (Fig. 4D and E). This phenomenon is attributed to the release of active ions by Laponite. Previous research has indicated that β-TCP doped with Li can modulate bone immune cells to induce bone regeneration [50]. GelMA incorporated with silicon nanosheets has exhibited promising outcomes in both osteogenesis and angiogenesis [51]. Indeed, Mg also plays a crucial role in bone immune condition and bone repair [52]. This further supports the notion that in the composite hydrogel containing Laponite, 8 % concentration proves to be a superior choice.

To thoroughly evaluate the impact of functional hydrogel scaffolds on bone formation, we conducted a rat skull defect model experiment (Fig. 5A and B). GelMA and GelMA/8%Lap hydrogel stents were separately modified with Apt19s. Subsequently, mico-CT scans were conducted at 4 and 10 weeks postoperatively. The CT images revealed significantly enhanced bone repair following Apt19s modification compared to the unmodified group. Particularly notable was the pronounced performance observed in the GelMA$^{Apt19s}$/8%Lap group in the CT images (Fig. 5C). Subsequently, quantitative analysis of BV/TV, Tb.BMD and Tb.Th was conducted on the CT data. At both the 4th and 10th week marks, the BV/TV and Tb.BMD ratios were higher in the GelMA$^{Apt19s}$/8%Lap group compared to the GelMA/8%Lap group (Fig. 5D–F) (see Fig. 6).

Furthermore, H&E and Masson staining were performed on the skull tissue. The findings revealed that at 4 weeks post-surgery, a modest amount of new bone tissue was evident in the defect area within the GelMA$^{Apt19s}$, GelMA/8%Lap, and GelMA$^{Apt19s}$/8%Lap groups. Portions of the hydrogel scaffolds, without degradation, remained visible, while the remaining regions were substituted by fibrous tissue. In the blank group, bone growth was absent within the bone defect region, primarily characterized by an excess of fibrous tissue. After 10 weeks post-surgery, the skull tissue within the same group remained predominantly occupied by fibrous tissue. In contrast, both GelMA$^{Apt19s}$/8%Lap group and GelMA/8%Lap group exhibited the emergence of new bone tissue within the voids of the hydrogel scaffold. Particularly noteworthy was the substantial occurrence of new bone tissue observed within the GelMA$^{Apt19s}$/8%Lap group (Fig. 6). New bone tissue formation within the scaffold space was noted, along with the examination of OPN protein expression in cranial tissues across all groups via immunohistochemistry. Findings revealed that OPN expression across all groups was higher at 4 weeks post-surgery compared to 10 weeks post-surgery, with the GelMA$^{Apt19s}$/8%Lap group exhibiting the most pronounced expression. In the blank group, a lower number of positive cells were observed (Fig. S6). This is attributed to Lap ions triggering the expression of the bone-forming gene OPN in BMSCs during the early stages of osteogenesis. As osteogenesis progresses, mineralization becomes predominant. This observation indirectly suggests that the inclusion of Lap enhances GelMA bone-inducting capacity. Furthermore, functional modification with Apt19s notably enhances the ability to stimulate bone regeneration.

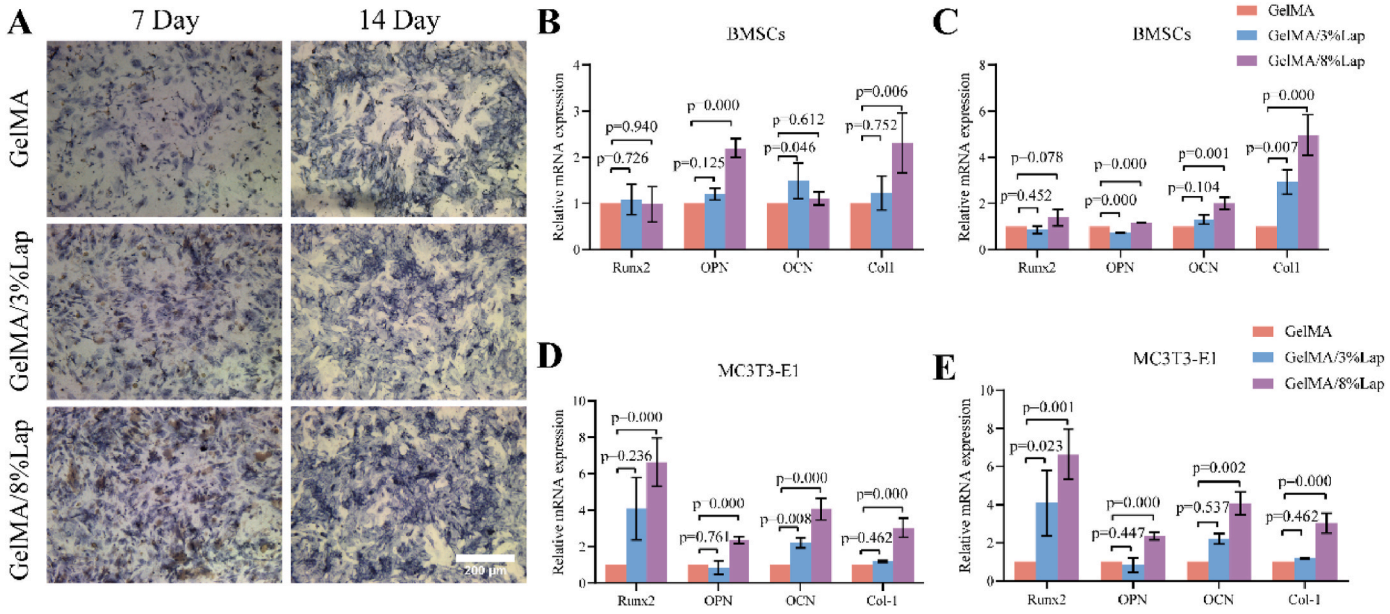


**Fig. 4.** Osteogenic differentiation assessment of 3D-printed hydrogel scaffolds. A. Representative images of ALP staining of BMSCs after 7 and 14 days of continuous induction with the extract of hydrogel scaffold. B. Evaluation of osteogenic gene expression (Col1, OPN, OCN, Runx2) in BMSCs cultured on various 3D-printed scaffolds for 7 days. C. Examination of osteogenic gene expression (Col1, OPN, OCN, Runx2) in BMSCs cells cultured on different 3D-printed scaffolds for 14 days. D. Evaluation of osteogenic gene expression (Col1, OPN, OCN, Runx2) in MC3T3 cells cultured on different 3D-printed scaffolds for 7 days. E. Analysis of osteogenic gene expression (Col1, OPN, OCN, Runx2) in MC3T3 cells cultured on different 3D-printed scaffolds for 14 days.

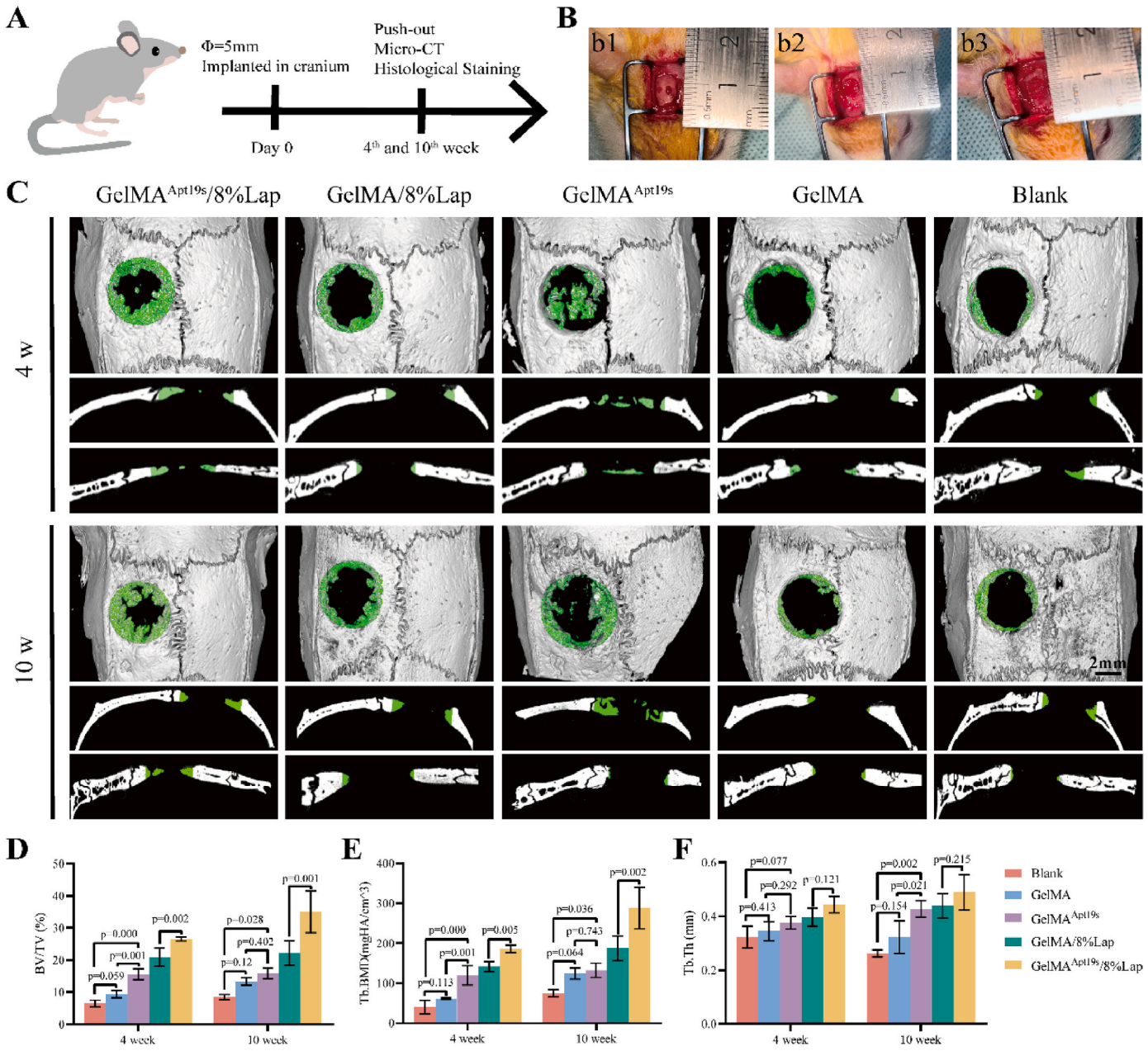


**Fig. 5.** Implantation of hydrogel scaffold for skull defect repair in rat experiments: A. Overall flow chart of animal experiments. B. Surgical procedures for hydrogel scaffold implantation. b1: Status of the complete skull. b2: Status of a 5 mm cranial defect. b3: Status after scaffold implantation. C. Micro-CT 3D reconstruction images of rat cranial defects implanted with the GelMA group, GelMA$^{Apt19s}$ group, GelMA/8%Lap group, and GelMA$^{Apt19s}$/8%Lap after surgery for 4 and 10 weeks, compared with the blank group. D. Quantitative analysis of bone volume fraction BV/TV in the repaired cranial defect area. E. Quantitative analysis of bone mineral density (BMD) in the repaired cranial defect area. F. Quantitative analysis of trabecular thickness (Tb.Th) in the repaired cranial defect area.

### *2.5. Hydrogel regulated osteogenic differentiation of BMSCs through the AMPK pathway*

Macrophages play a crucial role in bone regeneration through various mechanisms, including their response to Mg ions. The NF-κB pathway regulates the osteogenic differentiation of mesenchymal stem cells [53]. Additionally, Si can inhibit osteoclast activity and restore bone balance via the RANK pathway [54]. To investigate how composite hydrogel scaffolds can augment bone regeneration through macrophages, we initially induced bone immune conditions in the RM2 group for BMSCs culture for 7 days. Subsequently, ALP staining was conducted to assess the outcome. In comparison to the mere osteogenic induction medium, ALP staining was notably elevated in the RM2 group (Fig. 7A). Subsequently, PCR was employed to assess the expression of two-component bone genes. The findings revealed that the expressions of Runx2, OPN, ALP, and BMP-2 were higher in the RM2 group compared to the control group (Fig. 7B).

To elucidate the biological mechanism underlying the role of GelMA/Lap in regulating bone regeneration via bone immunity, RNA-seq sequencing was employed for analysis. The results revealed that under the influence of RM2 macrophage supernatant, there were 535 up-regulated differential genes and 990 down-regulated differential genes in BMSCs (Fig. 7C). GO and KEGG analyses of the differential genes were conducted in conjunction with the database. The findings revealed that some of the up-regulated enrichment genes were linked to osteogenic differentiation, chondrogenesis, and cranial macrophages during BP. In the KEGG analysis, the three most up-regulated pathways were cell cycle, ECM-receptor interaction, and focal adhesion pathways.

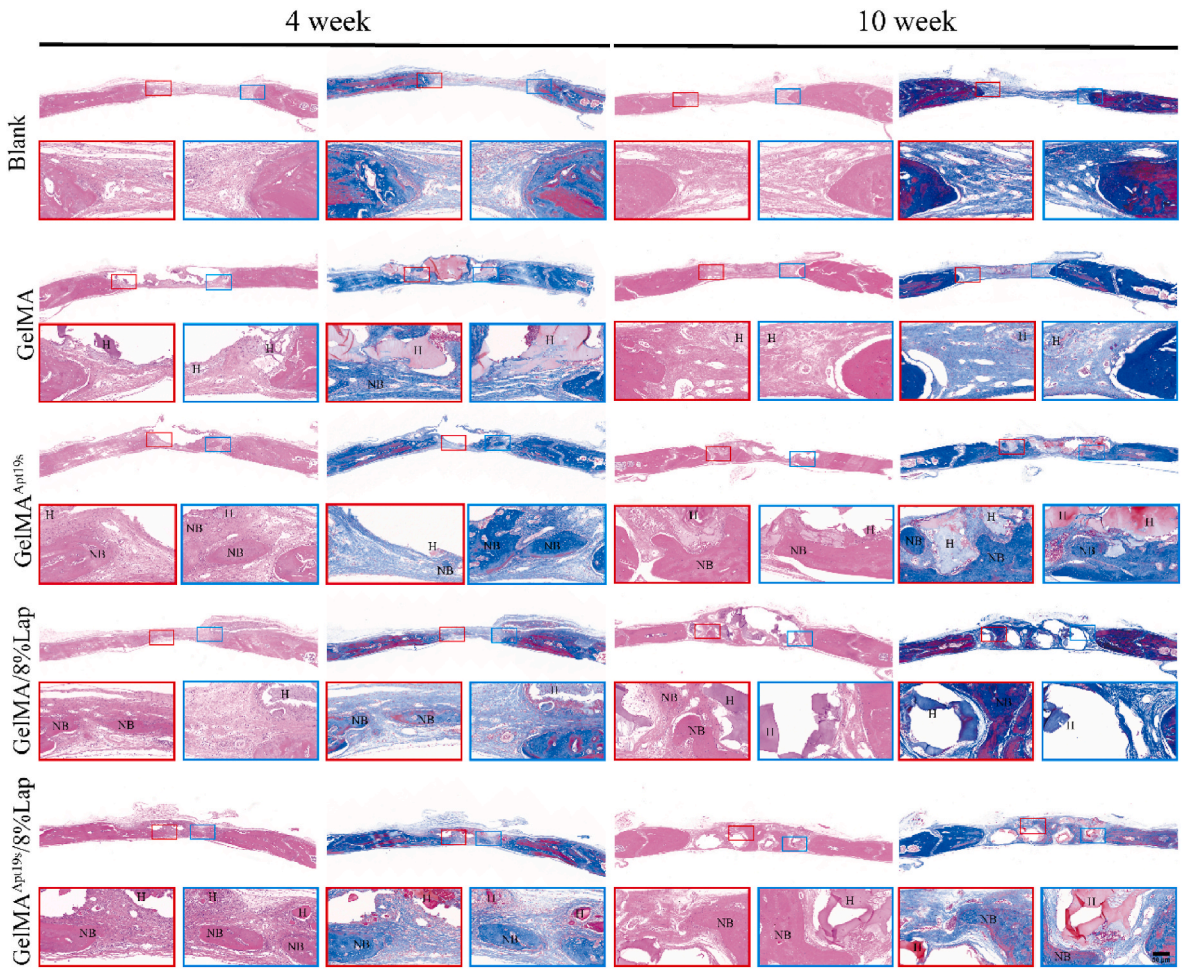


**Fig. 6.** Histological evaluations of cranial defect regeneration after 4 and 10 weeks of surgery. Representative H&E and Masson staining histological images of blank, GelMA, GelMA$^{Apt19s}$, GelMA/8%Lap, and GelMA$^{Apt19s}$/8%Lap (NB: new bone; H: hydrogel).

The most significant downgrades are TGF-beta signaling pathway, and Herpes simplex virus 1 infection (Fig. S7).

We also performed GSEA enrichment scores for all signaling pathways. The findings indicated that the AMPK pathway exhibited the most significant difference in BMSCs following intervention with RM2 supernatant (Fig. 7D). Previous research has demonstrated that increased phosphorylation of AMPK activates the downstream ULK1 autophagy axis, thereby facilitating osteogenic differentiation and enhancing bone repair [55]. As a crucial molecule within mammalian cells, mTOR participates in numerous biological processes and is also regulated by the phosphorylation level of AMPK. Studies have shown that PPARβ/δ accelerates bone regeneration in diabetes by augmenting autophagy through the AMPK/mTOR pathway [25]. Based on the sequencing analysis in this study, it was inferred that the macrophage supernatant might regulate the osteogenic differentiation of BMSCs through the AMPK/mTOR pathway. BMSCs were treated with the AMPK-specific inhibitor compound C. The results demonstrated a significant increase in the phosphorylation level of AMPK following the addition of macrophage supernatant. Simultaneously, the expression level of the bone formation-related protein BMP-2 showed a significant increase. However, following the administration of the AMPK inhibitor, the phosphorylation of AMPK, the phosphorylation level of mTOR and the expression of BMP-2 protein were markedly decreased (Fig. 7E–H). The findings suggest that the macrophage supernatant can enhance bone regeneration by activating the AMPK/mTOR pathway. However, inhibiting AMPK significantly weakened the osteogenic effect. In summary, the regulation of bone regeneration by composite hydrogel scaffolds through macrophages primarily occurs via the AMPK/mTOR pathway.

## 3. Experiment section

### 3.1. Materials

Fetal bovine serum (FBS), DMEM/F12 medium, DMEM/High glucose medium, phosphate buffered saline (PBS) and penicillin-streptomycin (PS) were obtained from Gibco (USA). Additionally, fluorescein phalloidin, M-CSF, IL-4, LPS, and γ-INF were obtained from MedChemExpress (MCE, USA). The proteins BMP-2, AMPK, phospho-AMPKα (Thr172), mTOR, phospho-mTOR (Ser2481), and β-actin were received from CST (USA). β-sodium glycerophosphate, dexamethasone, and ascorbic acid were obtained from Sigma-Aldrich (USA). Additionally, the BCIP/NBT alkaline phosphatase staining kit, BCA protein assay kit, and crystal violet were obtained from Beyotime (China). Histological reagents, including 4 % paraformaldehyde and 10 % EDTA solution, were received from Servicebio Technology (China). Anti-CD86, Anti-CD206, and Anti-F4/80 antibodies were acquired from Thermo Fisher Scientific (USA). GelMA (EFL-GM-60) was received from EngineeringForLife (China), while Laponite was obtained from Sigma (USA). 1-ethyl-3-(3-dimethyllamino-propyl) carbodiimide hydrochloride (EDC, AR) and N-hydroxysuccinimide (NHS, AR) were received from Aladdin (China). The aptamers utilized in this study were synthesized by Shangya (China), and their sequences are listed in Table S1.

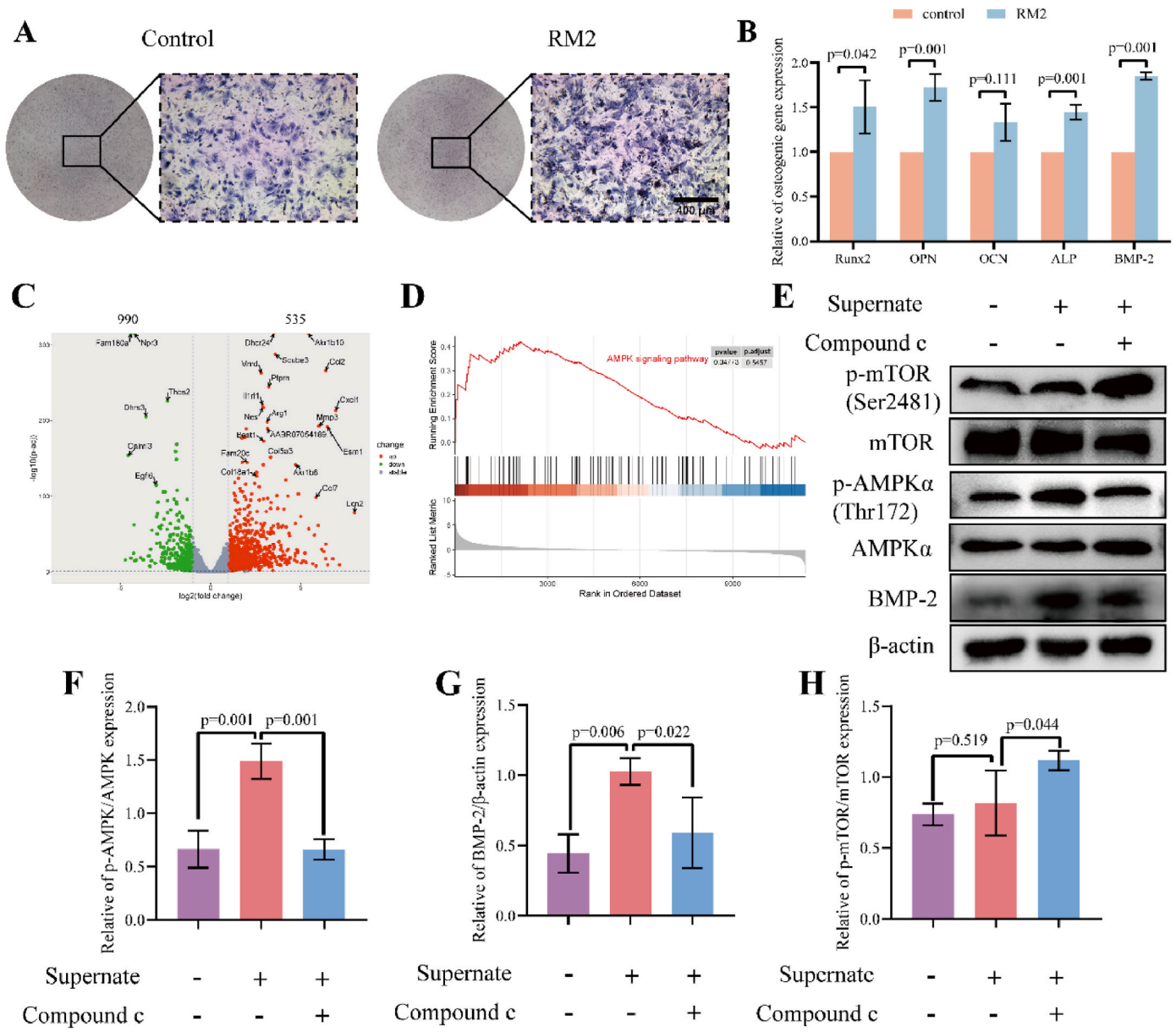


**Fig. 7.** A. Representative images displaying ALP staining of BMSCs after 7 days of continuous induction with RM2 macrophage supernatant. B. qRT-PCR analysis of mRNA levels of BMP-2, Runx2, OPN, ALP, and OCN in BMSCs treated with RM2 macrophages supernatant. C. Image depicting the volcano plot of the differentially expressed genes (DEGs) analysis in BMSCs continuously induced with RM2 macrophage supernatant compared to osteogenic induction medium. D. GSEA demonstrating a significant increase in the AMPK pathway gene enrichment score in RM2-induced BMSCs. E. Western blot analysis of protein levels of BMP-2, AMPK, phospho-AMPKα (Thr172), mTOR, phosph-mTOR (Ser2481), and β-actin.

### *3.2. Preparation of GelMA/Laponite hydrogel and 3D printed scaffold*

To prepare the GelMA/Laponite hydrogel and 3D-printed scaffold, the GelMA solid was first weighed and dissolved in PBS containing 0.25 % LAP initiator, resulting in a final concentration of 15 % solution. Subsequently, varying amounts of Laponite were added to the GelMA solution at concentrations of 3 % and 8 % (w/v). This mixture was agitated at 400 rpm for 2 h at 37 °C, ensuring that the environment was protected from light. The printing settings were configured as follows: layer height was set to 0.7 mm, line width was set to 0.7 mm, printing speed was ranging from 5 to 10 mm/s, extrusion rate was ranging from 6 to 9 $mm^3$/min, and the extrusion pressure was maintained at 0.1 MPa. Subsequently, the printed material was subjected to UV curing for 1 min using a UV lamp.

### *3.3. Characterization of 3D printed scaffold*

The entire hydrogel scaffold was photographed using a stereo microscope (SZ650, CNoptec). The internal structure of the hydrogel was examined using a scanning electron microscope (SEM). To prepare the sample for SEM, a section of the gel was cut, and its surface was coated with gold for 90 s before being removed. The observations were conducted using a Hitachi S-4800 SEM. Concurrently, elemental mapping was employed to analyze the content of Ca, Mg, C, Si, and O. The hydrogel underwent freeze-drying and was subsequently ground into a powder with a particle diameter of less than 80 μm, achieving uniformity through sifting with an 80-mesh screen. Fourier transform infrared spectroscopy (FTIR) was conducted using a Nicolet 5700 intelligent spectrometer with potassium bromide (KBr) as the testing medium, and scanning was carried out in the range of 400–4000 $cm^{-1}$. Additionally, X-ray diffraction (XRD) (Rigaku, Japan) was performed to determine the

crystallinity. XRD analysis was conducted using Cu radiation, with a scanning rate of 5°/min, across a range of 5–90°. Mechanical properties were assessed using a universal testing machine. Compression tests were performed at a speed of 1 mm/cm. Based on the obtained data, a compression-stress curve was plotted, and the compression modulus was subsequently calculated. The rheological tests were conducted using a rheometer in oscillatory mode, employing a flat plate probe with a diameter of 25 mm for the tests. In frequency mode scanning, the hydrogels were tested over a frequency range of 0.1–70 rad/s with a constant shear strain of 1 %. All experiments were performed at 37 °C. The GelMA/8%Laponite hydrogel scaffold were immersed in a 0.05 M Tris-HCl (pH = 7.4) buffer and then put in a constant temperature oven at 37 °C. Then plasma emission spectrometer (ICP, Optima 8000, Perkin Elmer) were used to measure the $Mg^{2+}$ concentration during the different time.

### 3.4. Conjugation of the scaffold with Apt19s

To conjugate the scaffold with Apt-19s, first, the hydrogel scaffold was submerged in a 2 ml buffer solution. Then, 8 mg of EDC and 12 mg of NHS were added. These compounds react with the carboxyl groups present on the surface of the scaffold. This reaction occurs at room temperature and typically lasts for 20 min, activating the carboxyl groups for further conjugation with the desired molecules. Once the reaction solution was discarded, the scaffold was washed twice with PBS. Subsequently, 6 ml of PBS was added to immerse the scaffold fully. Then, 10 nmol of amino-modified Apt19s was introduced into the PBS solution and allowed to react in a shaker set at 4 °C for 12 h. Following this reaction, the aptamer-modified hydrogel scaffold was obtained by thoroughly rinsing it twice with an MES coupling buffer.

### 3.5. Cell culture and macrophages polarization

MC3T3-E1 cells were procured from the National Collection of Authenticated Cell Cultures, China (Catalog: SCSP-5218). These cells were cultured in α-MEM supplemented with 10 % FBS. BMSCs were isolated from the femur of SD rats. Following the euthanasia of the SD rats, the intact femur was extracted, and both ends were removed for further processing. The femoral bone marrow cavity was continuously flushed with DMEM/F-12 supplemented with 20 % FBS and 1 % penicillin-streptomycin. The flushed solution was then filtered and centrifuged using a 70 μm cell sieve. The resulting cell suspension was resuspended in fresh medium and inoculated for further culture. Bone marrow-derived primary macrophages were isolated from BALB/c mice following euthanasia. The intact femur and tibia were isolated, and the ends of both bones were removed. Subsequently, the femoral bone marrow cavity was continuously flushed with high-glucose DMEM supplemented with 10 % FBS and 1 % penicillin-streptomycin. The rinsing solution was then filtered and centrifuged using a 70 μm cell sieve. After precipitation and resuspension, the fresh medium was inoculated for further cell culture. Following continuous induction with 20 ng/ml of M-CSF until day 7, the cells were stimulated to differentiate into M2 macrophages using 20 ng/ml of IL-4. Additionally, they were polarized into M1 macrophages with a combination of 20 ng/ml of INF-γ and 100 ng/ml of LPS.

### 3.6. Flow cytometry

BMSCs were digested and centrifuged, and the resulting cell pellet was collected. The cells were then treated with 200 μl of buffer A (adding 1 mg/mL BSA and 10 % FBS into D-PBS containing 4.5 mg/mL glucose and 5 mM $MgCl_2$), which contained a suspension of 10 nm FITC-Apts19s. After treatment, the cells were incubated at 37 °C for 1 h in a light-protected environment. Subsequently, they were washed three times with buffer B (adding 0.1 % $NaN_3$ into D-PBS containing 4.5 mg/mL glucose and 5 mM $MgCl_2$). Following this, flow cytometry was carried out after suspending in PBS. Additionally, M1 macrophages were cultured with GelMA/8%Lap hydrogel extract for 48 h, and this condition was marker as RM2. After digestion and collection of M1, M2, and RM2 primary macrophages, they were incubated with primary antibodies against CD86 and F4/80 primary for 30 min. Following washing with PBS, the cells were fixed with 4 % paraformaldehyde and permeabilized. Subsequently, the CD206 antibody was applied and incubated for 30 min in the absence of light. After washing off unbound antibodies, the cells were suspended in PBS for flow cytometry detection.

### 3.7. Immunofluorescence

For immunofluorescence analysis, primary macrophages were seeded onto coverslips and induced to M1, M2, and RM2 states. Following the removal of the medium, the cells were fixed with 4 % paraformaldehyde for 15 min. After washing with PBS, nonspecific binding sites were blocked with 5 % BSA for 30 min. Subsequently, the cells were incubated with the primary antibody CD86 at 4 °C overnight. After fixation, cell membranes were permeabilized with 0.3 % Triton-x-100. Subsequently, nonspecific binding sites were blocked with 5 % BSA for 30 min. The cells were then incubated with the primary antibody CD206 at 4 °C overnight. On the following day, the cells were washed three times with PBS-Tween (PBST), where each wash was carried out for 10 min. FITC-conjugated secondary antibody was added and incubated with the cells. After three additional washes with PBST, DAPI staining solution was added for 5 min to visualize the nuclei. Finally, a fluorescence microscope was used to observe the stained cells.

### 3.8. PCR

Total RNA was extracted from M1, M2, and RM2 primary macrophages using the Trizol method. Subsequently, 1.0 μg of total RNA was utilized for reverse transcription to generate cDNA. Upon completion of reverse transcription, the cDNA template was diluted five-fold with DEPC water for use in subsequent PCR experiments. Following the protocol, SYBR Green PCR Master Mix, cDNA, forward and reverse primers, and nuclease-free water were added in a total volume of 20 μl. The experimental results were quantified using the $2^{-\Delta\Delta ct}$ method, with GAPDH serving as the internal reference gene. Primer sequences are provided in Table S2.

### 3.9. Cell viability

Cell viability was assessed by culturing BMSCs cells in 24-well plates and treating them with hydrogel extract for 1 and 3 days. Following this, cells were washed with pre-cooled PBS and stained with Calcin-AM/PI dyeing solution, followed by a 15 min incubation away from light. Fluorescence microscope images were captured after further washing with PBS. BMSCs were seeded onto the GelMA scaffold and allowed to be cultured for 24 h. Subsequently, the cells were fixed with 4 % paraformaldehyde for 15 min and stained with fluorescein phalloidin solution. Following incubation at 37 °C, the cells were washed with PBST and stained with DAPI solution for 10 min. After three washes with PBST, the cell morphology was examined using confocal laser scanning.

### 3.10. Osteogenic differentiation

The hydrogel extract was prepared by supplementing 5 ml of osteogenic induction medium for every 200 μl of hydrogel. BMSCs cells and MC3T3 cells were seeded in 6-well plates at a density of $10^5$ cells. Then cultured for 7 and 14 days with the hydrogel extract replaced every 24 h continuously. Total RNA was extracted using the Trizol method, and the expression of osteogenic genes was assessed through reverse transcription and PCR. BMSCs cells were seeded in 12-well plates and cultured with extracts for 7 and 14 days. After incubation, the cells were fixed

with 4 % paraformaldehyde for 15 min, followed by staining with ALP dyeing solution for 20 min. Subsequently, the staining results were observed under a microscope. The supernatant from the RM2 group macrophages was collected. The bone immune-induced medium was prepared by combining it in a 1:2 ratio with an osteogenic induction medium. Subsequently, bone differentiation was assessed through ALP staining and PCR analysis on the 7th day following co-culture with BMSCs.

### 3.11. RNA-seq

RNA-seq analysis was conducted on bone immune-induced BMSCs established using the same method, with simple BMSCs serving as the control group. Total RNA was extracted and sequenced using the Illumina platform. The expression levels of genes were quantified using the RPKM (Reads Per Kilobase per Million mapped reads) value. Heatmaps and volcano plots were generated to illustrate the differences in gene expression between the groups. KEGG (Kyoto Encyclopedia of Genes and Genomes) and GO (Gene Ontology) analyses were employed to investigate the signal transduction pathways and biological functions associated with differentially expressed genes. Additionally, the GSEA method was utilized to evaluate the enrichment of differentially expressed significant signaling pathway molecules.

### 3.12. In vitro cell migration assay

Transwell system (Corning, USA) was employed to evaluate the *in vitro* recruitment ability of BMSCs by the Apt19s functionalized hydrogel scaffold. We conducted aptamer modification on GelMA and GelMA/8% Lap, while the unmodified scaffold served as the control group. In brief, $1 \times 10^4$ cells suspended in 400 μL of serum-free DMEM/F-12 were added to the upper chamber, while the scaffolds were placed in the lower chamber containing 2 mL of DMEM/F-12 with 5 % FBS and incubated for 6 h at 37 °C. Subsequently, the cells on the outer bottom surface of the upper chamber were fixed with 4 % paraformaldehyde, stained with crystal violet, and imaged under a light microscope. The number of cells in each field of view was then counted for statistical analysis.

### 3.13. Western blot

BMSCs were seeded in 6 cm dishes. One group was treated with bone immune-induced medium, while another group was treated with bone immune-induced medium along with AMPK specific inhibitor Compound C (1 μM). The control group was cultured with pure osteogenic induction medium for 3 days. The medium was discarded, and the cells were washed once with pre-cooled PBS. Subsequently, the cells were lysed by adding RIPA Lysis Buffer to the dish and placed on ice for 30 min. After cell lysis, the mixture was centrifuged at 12,000×*g* for 15 min at 4 °C. The proteins present in the supernatant were extracted, and protein quantification was conducted using the BCA method. Following protein extraction and quantification, SDS-PAGE gel electrophoresis was conducted, and the proteins were subsequently electrically transferred to a PVDF membrane. The membrane was then blocked with skim milk powder for 2 h and subsequently incubated overnight with a specific primary antibody at 4 °C. The following day, the membrane was washed three times with PBST for 10 min each wash, after which HRP was added to label the secondary antibody. The membrane was then incubated at room temperature for 1 h and washed three times with TBST for 10 min each wash. Subsequently, an ECL luminescent solution was added, and protein expression was detected using a chemiluminescence analyzer. The Image J software was utilized to analyze the gray values of protein expression for each group, and semi-quantitative statistical analysis was conducted.

### 3.14. Animal modeling

All animal experiments conducted in this study received approval from the Ethics Committee of Fujian Medical University (FJMU IACUC 2023–0165). 24 Sprague Dawley (SD) rats were randomly allocated into three groups. Following intraperitoneal injection, an incision was made in the skin on both sides of the thigh, and three groups of hydrogels (GelMA, GelMA/3%Lap, GelMA/8%Lap) were implanted beneath the skin. The skin wound was subsequently disinfected and sutured. Samples were collected on the 10th and 20th days post-surgery. An additional 40 SD rats were randomly assigned to 5 groups: Blank, GelMA, GelMA$^{Apt19s}$, GelMA/8%Lap, and GelMA$^{Apt19s}$/8%Lap. Following abdominal injection anesthesia, a 5 cm incision was made along the middle of the skull, and the periosteal tissue was entirely removed. A 5 mm diameter defect was then drilled using a high-speed abrasive drill, and the 3D-printed hydrogel was implanted. Finally, the wound was sutured.

### 3.15. Micro-CT analysis

Rats were euthanized via $CO_2$ asphyxiation at 4th and 10th weeks post-operation. The skulls were extracted and subjected to scanning using a micro-CT scanner. The acquired data underwent further processing using software to generate 3D images. Parameters such as BV/TV, Tb.Th, and Tb.BMD values within the ROI were indicative of the extent of new bone formation based on the micro-CT reconstruction data.

### 3.16. Histological staining

The hydrogel implanted into the subcutaneous tissue was removed via $CO_2$ asphyxiation at 10th and 20th days post-operation. The subcutaneous hydrogel, along with a small portion of surrounding tissue, was fully excised and fixed using 4 % paraformaldehyde. Subsequently, paraffin-embedded sections were prepared, followed by xylene treatment, gradient alcohol hydration, and staining with both Hematoxylin and Eosin (HE) and Masson staining, respectively. Following scanning, the CT tissue underwent continuous decalcification using a phosphate solution containing 12.5 % disodium EDTA. The solution was refreshed every 48 h. After complete decalcification, the tissue was paraffin-embedded and sectioned for further analysis. After treatment with xylene and gradient alcohol, the sections were subjected to antigen retrieval using sodium citrate. Endogenous peroxidase was blocked using hydrogen peroxide, followed by blocking with BSA (bovine serum albumin). Then, specific primary antibodies were added and incubated overnight at 4 °C. The following day, the sections were washed with PBS, and a secondary antibody polymer was applied. DAB (3,3′-diaminobenzidine) color development was carried out, followed by hematoxylin counterstaining and sealing with neutral gum.

### 3.17. Statistical analysis

Data analysis and plotting were conducted using SPSS 22.0 and Origin 2018. Experimental results were expressed as mean ± standard deviation. Comparisons among multiple groups were performed using one-way ANOVA followed by the LSD test. RNA transcriptome analysis and visualization were carried out using R language (version 4.3.1) along with related packages, including the DESeq package, ggplot package, and ComplexHeatmap package. Each *in vivo* and *in vitro* group experiment was repeated three times.

## 4. Conclusion

In this study, we conducted the first chemical modification of Apt19s on 3D-printed GelMA/Lap hydrogel scaffolds. As a result, the scaffolds exhibited an enhanced ability to recruit BMSCs. Through *in vitro* experiments, we not only confirmed the excellent biocompatibility of the

hydrogel scaffolds but also highlighted the remarkable affinity of Apt19s for BMSCs. This led to increased adhesion of BMSCs to the scaffold and facilitated their migration towards it. Functionally modified GelMA/8 % Lap exhibited a robust osteogenic effect both *in vivo* and *in vitro*. Moreover, the Lap-containing hydrogel scaffolds were observed to induce a reversal of macrophage polarization from M1 to M2. It was further observed that the secreted factors from these macrophages were found to regulate BMSCs osteogenic differentiation through the AMPK/mTOR signaling axis. In summary, Apt19s functionalized 3D-printed hydrogel scaffolds present a cost-effective and efficient solution for personalized, in situ repair of bone defects. Additionally, their molecular biological mechanism of inducing stem cell differentiation can provide a solid theoretical basis for clinical application.

## CRediT authorship contribution statement

**Linquan Zhou:** Writing – original draft, Software, Project administration, Funding acquisition, Formal analysis, Data curation. **Chengcheng Zhang:** Methodology, Formal analysis, Data curation, Conceptualization. **Tengbin Shi:** Software, Methodology, Data curation, Conceptualization. **Dingwei Wu:** Visualization, Software, Methodology. **Huina Chen:** Validation, Methodology, Data curation. **Jiaxin Han:** Supervision, Software, Project administration, Investigation. **Dehui Chen:** Software, Resources. **Jinxin Lin:** Writing – review & editing, Project administration, Conceptualization. **Wenge Liu:** Writing – review & editing, Writing – original draft, Project administration, Funding acquisition.

## Declaration of competing interest

The authors declare that they have no known competing financial interests or personal relationships that could have appeared to influence the work reported in this paper.

## Data availability

Data will be made available on request.

## Acknowledgements

This work is financially supported by National Natural Science Foundation of China (82072407), Fujian Provincial Health Technology Project (2021CXA013, 2023GGA014), and Fujian Provincial Natural Science Foundation of China (2023J05039).

## Appendix A. Supplementary data

Supplementary data to this article can be found online at https://doi.org/10.1016/j.mtbio.2024.101261.

## References

[1] A.H. Schmidt, Autologous bone graft: is it still the gold standard? Injury 52 (Suppl 2) (2021) S18–s22.
[2] Y. Zhu, B. Kong, R. Liu, Y. Zhao, Developing biomedical engineering technologies for reproductive medicine, Smart Medicine 1 (1) (2022) e20220006.
[3] H.J. Haugen, S.P. Lyngstadaas, F. Rossi, G. Perale, Bone grafts: which is the ideal biomaterial? J. Clin. Periodontol. 46 (Suppl 21) (2019) 92–102.
[4] N. Yamamoto, K. Hayashi, H. Tsuchiya, Progress in biological reconstruction and enhanced bone revitalization for bone defects, J. Orthop. Sci. : official journal of the Japanese Orthopaedic Association 24 (3) (2019) 387–392.
[5] W.C. Cuidi Li, 3D bioprinting of cell-laden constructs for regenerative medicine, Engineered Regeneration 2 (2021) 195–209.
[6] X.X. Chang Liu, Wenguo Cui, Hongbo Zhang, Metal-organic framework (MOF)-based biomaterials in bone tissue engineering, Engineered Regeneration 2021 (2) (2021) 105–108.
[7] H. Lin, L. Zhang, Q. Zhang, Q. Wang, X. Wang, G. Yan, Mechanism and application of 3D-printed degradable bioceramic scaffolds for bone repair, Biomater. Sci. 11 (21) (2023) 7034–7050.
[8] R. Liang, Y. Gu, Y. Wu, V. Bunpetch, S. Zhang, Lithography-based 3D bioprinting and bioinks for bone repair and regeneration, ACS biomaterials science & engineering 7 (3) (2021) 806–816.
[9] F. Lin, Y. Li, W. Cui, Injectable hydrogel microspheres in cartilage repair, Biomedical Technology 1 (2023) 18–29.
[10] S. Abbasnezhad, E. Biazar, F. Aavani, M. Kamalvand, S. Heidari Keshel, B. Pourjabbar, Chemical modification of acellular fish skin as a promising biological scaffold by carbodiimide cross-linker for wound healing, Int. Wound J. 20 (5) (2023) 1566–1577.
[11] T. Sun, C. Meng, Q. Ding, K. Yu, X. Zhang, W. Zhang, W. Tian, Q. Zhang, X. Guo, B. Wu, Z. Xiong, In situ bone regeneration with sequential delivery of aptamer and BMP2 from an ECM-based scaffold fabricated by cryogenic free-form extrusion, Bioact. Mater. 6 (11) (2021) 4163–4175.
[12] H. Li, T. Zhao, F. Cao, H. Deng, S. He, J. Li, S. Liu, Z. Yang, Z. Yuan, Q. Guo, Integrated bioactive scaffold with aptamer-targeted stem cell recruitment and growth factor-induced pro-differentiation effects for anisotropic meniscal regeneration, Bioengineering & Translational Medicine (2022).
[13] T. Sun, Z. Feng, W. He, C. Li, S. Han, Z. Li, R. Guo, Novel 3D-printing bilayer GelMA-based hydrogel containing BP,β-TCP and exosomes for cartilage-bone integrated repair, Biofabrication 16 (1) (2023).
[14] K. Man, I.A. Barroso, M.Y. Brunet, B. Peacock, A.S. Federici, D.A. Hoey, S.C. Cox, Controlled release of epigenetically-enhanced extracellular vesicles from a GelMA/nanoclay composite hydrogel to promote bone repair, Int. J. Mol. Sci. 23 (2) (2022).
[15] S.M. Mihaila, A.K. Gaharwar, R.L. Reis, A. Khademhosseini, A.P. Marques, M. E. Gomes, The osteogenic differentiation of SSEA-4 sub-population of human adipose derived stem cells using silicate nanoplatelets, Biomaterials 35 (33) (2014) 9087–9099.
[16] S. Miao, J. Zhou, B. Liu, X. Lei, T. Wang, X. Hao, P. Cheng, H. Wu, Y. Song, G. Pei, L. Bi, A 3D bioprinted nano-laponite hydrogel construct promotes osteogenesis by activating PI3K/AKT signaling pathway, Materials today. Bio 16 (2022) 100342.
[17] Y. Niu, Z. Wang, Y. Shi, L. Dong, C. Wang, Modulating macrophage activities to promote endogenous bone regeneration: biological mechanisms and engineering approaches, Bioact. Mater. 6 (1) (2021) 244–261.
[18] J. Pajarinen, T. Lin, E. Gibon, Y. Kohno, M. Maruyama, K. Nathan, L. Lu, Z. Yao, S. B. Goodman, Mesenchymal stem cell-macrophage crosstalk and bone healing, Biomaterials 196 (2019) 80–89.
[19] S.D. Dutta, K. Ganguly, T.V. Patil, A. Randhawa, K.T. Lim, Unraveling the potential of 3D bioprinted immunomodulatory materials for regulating macrophage polarization: state-of-the-art in bone and associated tissue regeneration, Bioact. Mater. 28 (2023) 284–310.
[20] R. Gruber, Osteoimmunology: inflammatory osteolysis and regeneration of the alveolar bone, J. Clin. Periodontol. 46 (Suppl 21) (2019) 52–69.
[21] Z. Chen, Z. Cai, P. Zhuang, F. Li, W. Cui, Z. Li, Living probiotic biomaterials for osteoporosis therapy, Biomedical Technology 1 (2023) 52–64.
[22] S. Chen, L. Tao, F. Zhu, Z. Wang, Q. Zhuang, Y. Li, Y. Yang, C. Feng, H. Shi, J. Shi, L. Zhu, L. Xiao, D. Geng, Z. Wang, BushenHuoxue decoction suppresses M1 macrophage polarization and prevents LPS induced inflammatory bone loss by activating AMPK pathway, Heliyon 9 (5) (2023) e15583.
[23] H. Wu, H. Dong, Z. Tang, Y. Chen, Y. Liu, M. Wang, X. Wei, N. Wang, S. Bao, D. Yu, Z. Wu, Z. Yang, X. Li, Z. Guo, L. Shi, Electrical stimulation of piezoelectric BaTiO3 coated Ti6Al4V scaffolds promotes anti-inflammatory polarization of macrophages and bone repair via MAPK/JNK inhibition and OXPHOS activation, Biomaterials 293 (2023) 121990.
[24] M. Arioka, F. Takahashi-Yanaga, M. Sasaki, T. Yoshihara, S. Morimoto, M. Hirata, Y. Mori, T. Sasaguri, Acceleration of bone regeneration by local application of lithium: Wnt signal-mediated osteoblastogenesis and Wnt signal-independent suppression of osteoclastogenesis, Biochem. Pharmacol. 90 (4) (2014) 397–405.
[25] M. Chen, D. Jing, R. Ye, J. Yi, Z. Zhao, PPARβ/δ accelerates bone regeneration in diabetic mellitus by enhancing AMPK/mTOR pathway-mediated autophagy, Stem Cell Res. Ther. 12 (1) (2021) 566.
[26] C. Cui, Z. Bao, S.K. Chow, R.M.Y. Wong, A. Welch, L. Qin, W.H. Cheung, Coapplication of magnesium supplementation and vibration modulate macrophage polarization to attenuate sarcopenic muscle atrophy through PI3K/Akt/mTOR signaling pathway, Int. J. Mol. Sci. 23 (21) (2022).
[27] X. Wei, Z. Tang, H. Wu, X. Zuo, H. Dong, L. Tan, W. Wang, Y. Liu, Z. Wu, L. Shi, N. Wang, X. Li, X. Xiao, Z. Guo, Biofunctional magnesium-coated Ti6Al4V scaffolds promote autophagy-dependent apoptosis in osteosarcoma by activating the AMPK/mTOR/ULK1 signaling pathway, Materials today. Bio 12 (2021) 100147.
[28] Q. Li, H. Yu, F. Zhao, C. Cao, T. Wu, Y. Fan, Y. Ao, X. Hu, 3D printing of microenvironment-specific bioinspired and exosome-reinforced hydrogel scaffolds for efficient cartilage and subchondral bone regeneration, Adv. Sci. 10 (26) (2023) e2303650.
[29] B. Zhou, X. Jiang, X. Zhou, W. Tan, H. Luo, S. Lei, Y. Yang, GelMA-based bioactive hydrogel scaffolds with multiple bone defect repair functions: therapeutic strategies and recent advances, Biomater. Res. 27 (1) (2023) 86.
[30] N.R. de Barros, A. Gomez, M. Ermis, N. Falcone, R. Haghniaz, P. Young, Y. Gao, A. F. Aquino, S. Li, S. Niu, R. Chen, S. Huang, Y. Zhu, P. Eliahoo, A. Sun, D. Khorsandi, J. Kim, J. Kelber, A. Khademhosseini, H.J. Kim, B. Li, Gelatin methacryloyl and Laponite bioink for 3D bioprinted organotypic tumor modeling, Biofabrication 15 (4) (2023).
[31] J.M. McCracken, B.M. Rauzan, J.C.E. Kjellman, M.E. Kandel, Y.H. Liu, A. Badea, L. A. Miller, S.A. Rogers, G. Popescu, R.G. Nuzzo, 3D-Printed hydrogel composites for predictive temporal (4D) cellular organizations and patterned biogenic mineralization, Adv. Healthcare Mater. 8 (1) (2019) e1800788.

[32] R. Zhang, L. Xie, H. Wu, T. Yang, Q. Zhang, Y. Tian, Y. Liu, X. Han, W. Guo, M. He, S. Liu, W. Tian, Alginate/laponite hydrogel microspheres co-encapsulating dental pulp stem cells and VEGF for endodontic regeneration, Acta Biomater. 113 (2020) 305–316.
[33] B.K. Heragh, S. Javanshir, G.R. Mahdavinia, M.R.N. Jamal, Hydroxyapatite grafted chitosan/laponite RD hydrogel: evaluation of the encapsulation capacity, pH-responsivity, and controlled release behavior, Int. J. Biol. Macromol. 190 (2021) 351–359.
[34] Y. Miao, X. Liu, J. Luo, Q. Yang, Y. Chen, Y. Wang, Double-network DNA macroporous hydrogel enables aptamer-directed cell recruitment to accelerate bone healing, Adv. Sci. 11 (1) (2024) e2303637.
[35] P. Guo, The emerging field of RNA nanotechnology, Nat. Nanotechnol. 5 (12) (2010) 833–842.
[36] G. Lokhande, J.K. Carrow, T. Thakur, J.R. Xavier, M. Parani, K.J. Bayless, A. K. Gaharwar, Nanoengineered injectable hydrogels for wound healing application, Acta Biomater. 70 (2018) 35–47.
[37] A.K. Gaharwar, L.M. Cross, C.W. Peak, K. Gold, J.K. Carrow, A. Brokesh, K. A. Singh, 2D nanoclay for biomedical applications: regenerative medicine, therapeutic delivery, and additive manufacturing, Advanced materials (Deerfield Beach, Fla.) 31 (23) (2019) e1900332.
[38] P. Shi, Y.H. Kim, M. Mousa, R.R. Sanchez, R.O.C. Oreffo, J.I. Dawson, Self-assembling nanoclay diffusion gels for bioactive osteogenic microenvironments, Adv. Healthcare Mater. 7 (15) (2018) e1800331.
[39] N.Y. Patrawalla, N.S. Kajave, V. Kishore, A comparative study of bone bioactivity and osteogenic potential of different bioceramics in methacrylated collagen hydrogels, Journal of biomedical materials research. Part A 111 (2) (2023) 224–233.
[40] Y. Li, D. Zhao, Z. Wang, Y. Meng, B. Liu, L. Li, R. Liu, S. Dong, F. Wei, Minimally invasive bone augmentation through subperiosteal injectable hydroxylapatite/laponite/alginate nanocomposite hydrogels, Int. J. Biol. Macromol. 231 (2023) 123232.
[41] H. Li, T. Zhao, F. Cao, H. Deng, S. He, J. Li, S. Liu, Z. Yang, Z. Yuan, Q. Guo, Integrated bioactive scaffold with aptamer-targeted stem cell recruitment and growth factor-induced pro-differentiation effects for anisotropic meniscal regeneration, Bioeng Transl Med 7 (3) (2022) e10302.
[42] X. Hu, Y. Wang, Y. Tan, J. Wang, H. Liu, Y. Wang, S. Yang, M. Shi, S. Zhao, Y. Zhang, Q. Yuan, A difunctional regeneration scaffold for knee repair based on aptamer-directed cell recruitment, Advanced materials (Deerfield Beach, Fla.) 29 (15) (2017).
[43] S. Chen, H. Wang, D. Liu, J. Bai, H.J. Haugen, B. Li, H. Yan, Early osteoimmunomodulation by mucin hydrogels augments the healing and revascularization of rat critical-size calvarial bone defects, Bioact. Mater. 25 (2023) 176–188.
[44] S.Y. Yang, Y.N. Zhou, X.G. Yu, Z.Y. Fu, C.C. Zhao, Y. Hu, K.L. Lin, Y.J. Xu, A xonotlite nanofiber bioactive 3D-printed hydrogel scaffold based on osteo-/angiogenesis and osteoimmune microenvironment remodeling accelerates vascularized bone regeneration, J. Nanobiotechnol. 22 (1) (2024) 59.
[45] J. Lee, H. Byun, S.K. Madhurakkat Perikamana, S. Lee, H. Shin, Current advances in immunomodulatory biomaterials for bone regeneration, Adv. Healthcare Mater. 8 (4) (2019) e1801106.
[46] C. Schlundt, H. Fischer, C.H. Bucher, C. Rendenbach, G.N. Duda, K. Schmidt-Bleek, The multifaceted roles of macrophages in bone regeneration: a story of polarization, activation and time, Acta Biomater. 133 (2021) 46–57.
[47] G. Jiang, S. Li, K. Yu, B. He, J. Hong, T. Xu, J. Meng, C. Ye, Y. Chen, Z. Shi, G. Feng, W. Chen, S. Yan, Y. He, R. Yan, A 3D-printed PRP-GelMA hydrogel promotes osteochondral regeneration through M2 macrophage polarization in a rabbit model, Acta Biomater. 128 (2021) 150–162.
[48] C. Yu, X. Dou, L. Meng, X. Feng, C. Gao, F. Chen, X. Tang, Structure, rheological properties, and biocompatibility of Laponite® cross-linked starch/polyvinyl alcohol hydrogels, Int. J. Biol. Macromol. 253 (Pt 8) (2023) 127618.
[49] R. Leu Alexa, A. Cucuruz, C.D. Ghițulică, G. Voicu, L.R. Stamat Balahura, S. Dinescu, G.M. Vlasceanu, C. Stavarache, R. Ianchis, H. Iovu, M. Costache, 3D printable composite biomaterials based on GelMA and hydroxyapatite powders doped with cerium ions for bone tissue regeneration, Int. J. Mol. Sci. 23 (3) (2022).
[50] K. Hurle, F.R. Maia, V.P. Ribeiro, S. Pina, J.M. Oliveira, F. Goetz-Neunhoeffer, R. L. Reis, Osteogenic lithium-doped brushite cements for bone regeneration, Bioact. Mater. 16 (2022) 403–417.
[51] C. Xu, Y. Chang, Y. Xu, P. Wu, C. Mu, A. Nie, Y. Qu, D. Duan, X. Guo, Z. Liu, J. Wang, Z. Luo, Silicon-phosphorus-nanosheets-Integrated 3D-printable hydrogel as a bioactive and biodegradable scaffold for vascularized bone regeneration, Adv. Healthcare Mater. 11 (6) (2022) e2101911.
[52] W. Qiao, K.H.M. Wong, J. Shen, W. Wang, J. Wu, J. Li, Z. Lin, Z. Chen, J. P. Matinlinna, Y. Zheng, S. Wu, X. Liu, K.P. Lai, Z. Chen, Y.W. Lam, K.M.C. Cheung, K.W.K. Yeung, TRPM7 kinase-mediated immunomodulation in macrophage plays a central role in magnesium ion-induced bone regeneration, Nat. Commun. 12 (1) (2021) 2885.
[53] M. Bessa-Gonçalves, A.M. Silva, J.P. Brás, H. Helmholz, B.J.C. Luthringer-Feyerabend, R. Willumeit-Römer, M.A. Barbosa, S.G. Santos, Fibrinogen and magnesium combination biomaterials modulate macrophage phenotype, NF-kB signaling and crosstalk with mesenchymal stem/stromal cells, Acta Biomater. 114 (2020) 471–484.
[54] L. Mao, L. Xia, J. Chang, J. Liu, L. Jiang, C. Wu, B. Fang, The synergistic effects of Sr and Si bioactive ions on osteogenesis, osteoclastogenesis and angiogenesis for osteoporotic bone regeneration, Acta Biomater. 61 (2017) 217–232.
[55] S. Zhang, Y. Xie, F. Yan, Y. Zhang, Z. Yang, Z. Chen, Y. Zhao, Z. Huang, L. Cai, Z. Deng, Negative pressure wound therapy improves bone regeneration by promoting osteogenic differentiation via the AMPK-ULK1-autophagy axis, Autophagy 18 (9) (2022) 2229–2245.